Analysis of AQP4 Trafficking Vesicle Dynamics Using a High-Content Approach

Javier Mazzaferri,[†] Santiago Costantino,[†‡*] and Stephane Lefrancois[†§*]
[†]Centre de Recherche de l'Hôpital Maisonneuve-Rosemont, Montréal, Canada; [‡]Département d'Ophtalmologie et Institut de Génie Biomédical, Université de Montréal, Montréal, Canada; and [§]Département de Médecine, Université de Montréal, Montréal, Canada

ABSTRACT Aquaporin-4 (AQP4) is found on the basolateral plasma membrane of a variety of epithelial cells, and it is widely accepted that microtubules play an important role in protein trafficking to the plasma membrane. In the particular case of polarized trafficking, however, most evidence on the involvement of microtubules has been obtained via biochemistry experiments and single-shot microscopy. These approaches have provided essential information, even though they neglect the dynamical details of microtubule transport. In this work, we present a high-content framework in which time-lapse imaging, and single-particle-tracking algorithms were used to study a large number (~10^4) of GFP-AQP4-carrying vesicles on a large number of cells (~170). By analyzing several descriptors in this large sample of trajectories, we were able to obtain highly statistically significant results. Our results support the hypothesis that AQP4 is transported along microtubules, but to our surprise, this transport is not directed straight to the basolateral plasma membrane. On the contrary, these vesicles move stochastically along microtubules, changing direction repeatedly. We propose that the role of microtubules in the basolateral trafficking of AQP4 is to increase the efficiency, rather than determine the specificity of the target.

INTRODUCTION

Polarized epithelial cells display two segregated plasma membrane domains: the apical surface, which faces the lumen, and the basolateral plasma membrane (BPM), which borders on the interstitial space. To maintain this polarity, cells sort and package specific proteins into trafficking vesicles that are then targeted to those membrane domains. The molecular mechanisms involved in localizing cargo to specific regions of the membrane are diverse, depend on cell type, the particular protein to be transported, and the membrane domain and are, in some cases, redundant (1,2). There is a consensus that in the biosynthetic pathway, newly synthesized membrane proteins are first gathered at the level of the Golgi apparatus (3), then sorted into distinct carriers in the trans-Golgi network (TGN) and subsequently delivered to specific membrane regions (4,5). How this delivery is made is not completely understood, but microtubules have been repeatedly reported to be required (1,6,7).

Aquaporins (AQPs) are water-permeable membrane channels found on the plasma membranes of cells. These evolutionarily conserved proteins are also found in bacteria and plants (8). Mammalian cells express 13 AQP isoforms, with AQPs 0, 1, 2, 4, 5, 6, and 8 being permeable only to water, whereas AQPs 3, 7, 9, and 10 are also permeable to small molecules such as urea and glycerol (9). AQPs are expressed in various tissue types, including lung, kidney, and brain, and serve to protect epithelial tissue from dehydration (10). Within polarized cells, AQPs can localize to specific membrane domains. For example, AQP3 and AQP4 traffic and are localized to the basolateral membrane (11,12), whereas AQP2 and AQP5 are found on the apical plasma membrane (9). Although the trafficking and localization of AQPs has been widely studied, with previous studies showing, for example, that two independent C-terminal signals determine the targeting of AQP4 to the basolateral membrane of cultured astrocytes (13) and Madin-Darby canine kidney (MDCK) cells (14), the molecular mechanisms are still not completely understood. Finally, it has been reported that AQP4 is constitutively phosphorylated in cultured astrocytes, which is required for Golgi transition of AQP4 (15), but it is not clear whether these signals direct AQP4 trafficking vesicles straight to the BPM from the Golgi.

Regardless, all of these previous trafficking studies were based on biochemical experiments and protein localization assessed by low-content approaches (13–19). Such approaches neglect the dynamic details of vesicular transport, and although the selective delivery of secretory cargo in Golgi-derived carriers was studied dynamically in nonepithelial cells (20), and the TGN-to-plasma-membrane traffic was addressed in nonpolarized cells (21), to the best of our knowledge, there are no studies of the dynamics of trafficking in apical-basolateral polarized cells using a high-content approach.

In this work, we present a high-content approach based on single-particle tracking (SPT) to analyze the dynamics of green-fluorescent-protein (GFP)-tagged AQP4 (GFP-AQP4) in polarized and nonpolarized MDCK cells. Using an automated approach, we were able to characterize the trafficking of a large number of vesicles ($N \sim 10^4$), which in turn provide the statistical significance of the results. Interestingly, we found that vesicles containing GFP-AQP4

Submitted March 8, 2013, and accepted for publication June 7, 2013.

*Correspondence: santiago.costantino@umontreal.ca or stephane.lefrancois@umontreal.ca

Editor: Rong Li.

0006-3495/13/07/0328/10 $2.00

http://dx.doi.org/10.1016/j.bpj.2013.06.010

are not directly transported from the Golgi to the BPM, suggesting that a yet undefined molecular mechanism within the BPM restricts the distribution of AQP4 to the area.

MATERIALS AND METHODS

Cell culture and transfection of GFP-AQP4

MDCK cells were transfected with GFP-AQP4 in 100-mm-diameter culture plates using Lipofectamine 2000 (Life Technologies, Burlington, ON, Canada). At 48 h posttransfection, the selective agent geneticin (G418 sulfate, Life Technologies) was added to a final concentration of 800 μg/ml. This concentration was previously shown to eliminate all nontransfected cells within 1 week. After 1 week, cells were split twice a week, always maintaining selective pressure with the G418 at 800 μg/ml. Stable cell lines were grown in MEM-α (Life Technologies) without nucleosides and supplemented with 10% fetal bovine serum (FBS), 50 units/ml penicillin, and 50 μg/ml streptomycin (all from Life Technologies) at 37°C and 5% CO_2.

The day before imaging, we plated cells on glass-bottomed dishes (MatTek, Ashland, MA). The experiments with polarized cells were prepared by seeding cells at a concentration four times that used for nonpolarized cells to increase the occurrence of intercellular contacts. Five minutes before imaging, the standard culture media was replaced with MEM-α without Phenol red, supplemented with 10% FBS and 20 mM Hepes (all from Life Technologies). During imaging, we kept the sample at 37°C with a PDMI-2 microincubator connected to a TC-202A temperature controller (both from Harvard Apparatus, Holliston, MA) mounted on the microscope stage.

Imaging

Samples were imaged using an epifluorescence inverted microscope (Olympus IX71, Richmond Hill, ON, Canada) equipped with a CCD camera (Retiga 2000R, Surrey, BC, Canada) and a 60× NA 1.35 oil-immersion objective. We used a custom program, coded in LabView (National Instruments, Austin, TX), to acquire images at fixed-frame rates ranging from 4 to 10 Hz with CCD exposure times ranging from 100 ms to 65 ms. The duration of imaging depended on GFP expression in each field of view and ranged from 1 to 5 min, but the number of frames was never lower than 240.

SPT algorithms

We implemented an SPT program, coded in MATLAB (The MathWorks, Natick, MA), based on Crocker and Grier's tracking algorithm (22). The software has two stages, detection and tracking. In the detection phase, we processed each frame in two steps. First, a bandpass spatial filter constrains the image size of the vesicles within the range 200–600 nm. This step not only reduces imaging noise and discards large structures but also rejects out-of-focus vesicles, yielding a digitally generated optical section (23). Second, the algorithm detects the local maxima positions and computes the centroid of neighbor pixels to increase the spatial resolution. The neighboring regions of each local maximum are also used for removing noise, as described below. Finally, in the tracking stage, vesicle coordinates are linked between consecutive frames to obtain the trajectories of each vesicle.

Data analysis

We used a set of four descriptors to evaluate the vesicular trajectories: time lag (t_{lag}), mean velocity ($<v>$), and two scalars, radius of gyration (R_g) and shape (A_2), derived from the gyration tensor, T (see description below). The time lag is simply the time interval within which each vesicle was tracked. To compute the mean velocity, the instantaneous velocity (v_i) was first computed for each frame by fitting the traveled distance versus time on four consecutive frames to a straight line (24). Finally, v_i was averaged along all frames within t_{lag} to obtain the mean velocity, $<v>$.

The gyration tensor, T, characterizes the extension and shape of the trajectory as described by Saxton (25). Basically,

$$T = \begin{pmatrix} T_{xx} & T_{xy} \\ T_{xy} & T_{yy} \end{pmatrix} = \begin{pmatrix} \langle x^2\rangle - \langle x\rangle^2 & \langle xy\rangle - \langle x\rangle\langle y\rangle \\ \langle xy\rangle - \langle x\rangle\langle y\rangle & \langle y^2\rangle - \langle y\rangle^2 \end{pmatrix}, \tag{1}$$

where x and y are the coordinates of the vesicle, and the averages (variables in angled brackets) are over all the frames in the trajectory. This tensor can be diagonalized, and its eigenvalues are the squared principal radii of gyration

$$R_1^2, R_2^2 = \frac{1}{2}\left[\left(T_{xx}+T_{yy}\right) \pm \sqrt{\left(T_{xx}-T_{yy}\right)^2 + 4\,T_{xy}^2}\right]. \tag{2}$$

From the eigenvalues in Eq. 2 we can define the squared radius of gyration and the shape parameter:

$$\begin{aligned} R_g^2 &= R_1^2 + R_2^2 \\ A_2 &= \frac{\left(R_1^2 - R_2^2\right)^2}{\left(R_1^2 + R_2^2\right)^2}. \end{aligned} \tag{3}$$

The ellipse of gyration has semiaxes R_1 and R_2 that provide a graphical representation of T. The parameters defined in Eq. 3 describe its geometry. R_g^2 measures the extension of the trajectory and A_2 describes the degree of asymmetry. For example, an isotropic trajectory results in a circular ellipse of gyration with $A_2 = 0$ ($R_1 = R_2$), whereas an elongated trajectory renders $A_2 = 1$, because either R_1 or R_2 goes to 0. For this reason, the statistical distribution of A_2 is specially suited to distinguish directed transport from random motion. The trajectories of randomly diffusing particles show a characteristic distribution of A_2, leaned against the axis $A_2 = 0$ (25). Instead, if the underlying transport is directed, the histogram is skewed to the right, representing an increased number of stretched trajectories ($A_2 \sim 1$). In the experiments below, we compare the histograms of A_2 under several conditions to assess differences in the vesicle's motion.

The standard approach to study particle dynamics upon SPT is to analyze the mean-square displacement (MSD) versus time-delay curve, and compare different models of movement. The MSD is defined for a time delay $n\Delta t$ as

$$\begin{aligned} \mathrm{MSD}(n\Delta t) &= \frac{1}{N-n}\sum_{i}^{N-n}\rho_i(n\Delta t) \\ \rho_i(n\Delta t) &= \left(x(t_i+n\Delta t)-x(t_i)\right)^2+\left(y(t_i+n\Delta t)-y(t_i)\right)^2 \end{aligned}, \tag{4}$$

where Δt is the time interval between consecutive frames and N is the total number of frames. It is known that the functional form of MSD(Δt) depends on the type of transport (26). For example, particles undergoing random diffusion yield an MSD that is a first-degree polynomial as

$$\mathrm{MSD}_{RD}(n\Delta t) = \frac{1}{6}D\,n\Delta t, \tag{5}$$

where D is the diffusion coefficient. Similarly, particles that combine directed motion and random diffusion are characterized by the second-degree polynomial MSD:

$$\mathrm{MSD}_{D}(n\Delta t) = \frac{1}{6}D\,n\Delta t + \left(v_D\,n\Delta t\right)^2, \tag{6}$$

where v_D is the directed-motion speed of the particle. Equations 5 and 6 are probably the simplest choices among a variety of models ranging from anomalous subdiffusion to several variants of confined movement. However, fitting the experimental MSD to these two elementary models is a simple approach to distinguish between random and directed motion.

In our experiments, we compute weighted least-square fits to first- and second-degree polynomials and choose the function that yields the lower χ^2 value. Each MSD ($n\Delta t$) value was weighted by the function

$$WG(n\Delta t) = \frac{1}{SE^2(n\Delta t)}, \quad (7)$$

where SE is the standard error, which we estimate as

$$SE(n\Delta t) = \frac{SD(\rho_i(n\Delta t))}{\sqrt{N-n}}, \quad (8)$$

and SD is the standard deviation. MSD curves were limited to 10-s delays and we always kept $n < N - 100$ for accuracy.

From a probabilistic perspective, Eq. 6 almost always gives a better fit because of its higher degree, even when the underlying model is Eq. 5. Therefore, we use an F-test to evaluate the probability that the decrease in χ^2 due to a better fit with Eq. 6 has occurred by chance (27). We consider that Eq. 6 has a better fit than Eq. 5 when the F-test yields $p < 0.0001$. Finally, a trajectory is regarded as directed motion when, besides fitting Eq. 6, v_D is at least as high as $0.2<v>$. The reliability of the fits is controlled by checking that integrated probability of χ^2 exceeding the experimental value ($P(>\chi^2)$) > 0.1 (27).

To quantify the directed motion of a set of trajectories we define the ratio

$$R_D = \frac{N_D}{N_{RD}}, \quad (9)$$

where N_{RD} and N_D are the number of trajectories corresponding to random diffusion and directed motion, respectively.

Noise handling

After tracking all trajectories, we used a particular set of descriptors to avoid tracks originating from noise or artifacts that may bias our conclusions. The trajectories resulting from random noise (false positives) are frequently very short in time, because the likelihood of these events occurring in sequential frames, in the same neighborhood and sustained in time, is low. Therefore, we reject most of these false trajectories by considering only vesicles tracked for >10 frames.

Static vesicles were also discarded from our analyses, but due to imaging noise, SPT on static objects often gave rise to trajectories that were difficult to identify as static. Nevertheless, these noisy trajectories seldom move away from the initial position and Rg^2 never surpasses a certain threshold. We determined this threshold value experimentally by imaging and tracking fluorescent beads immobilized to a glass coverslip for 30 s, at the same time matching the imaging parameters and signal/noise ratio of live-cell experiments. The histogram of Rg^2 for the resulting tracks is a bell-shaped curve in which >90% of the trajectories have values $<0.005\ \mu m^2$. In our experiments, we reject tracks with Rg^2 below this threshold to avoid static objects.

Finally, in some cases, the protein accumulation in the cell membrane gave rise to false vesicle detection that can't be rejected with the procedures described above. Generally, these false vesicles are big, so we eliminate them by further restricting the maximum allowed size of vesicles to a threshold below around 600 nm. We select the threshold specifically for each particular field of view because it depends on the shape of the cell membrane.

RESULTS

Validation of the SPT algorithm

We tested the ability of the proposed method to distinguish random from directed-motion trajectories by imaging the Brownian motion of fluorescent polyester beads in a liquid solution. A drop of fluorescent beads with an average diameter of 51 nm (Bangs Laboratories, Fichers, IN) suspended in glycerol was mounted between a coverglass and a microscope slide and imaged as described above at 10 fps for 250 s. To simulate a steady drift (directed motion), the motorized stage of the microscope slowly moved at a constant velocity during imaging. We imaged the sample while the stage moved at 0 μm/s, 0.2 μm/s, and 1 μm/s, and we processed these movies with the SPT algorithm described above (Fig. 1, *A–C*, and Movies S1–S3 in the Supporting Material). We found that the A_2 histogram (Fig. 1 *D*) for the pure Brownian movement (stage speed = 0 μm/s)

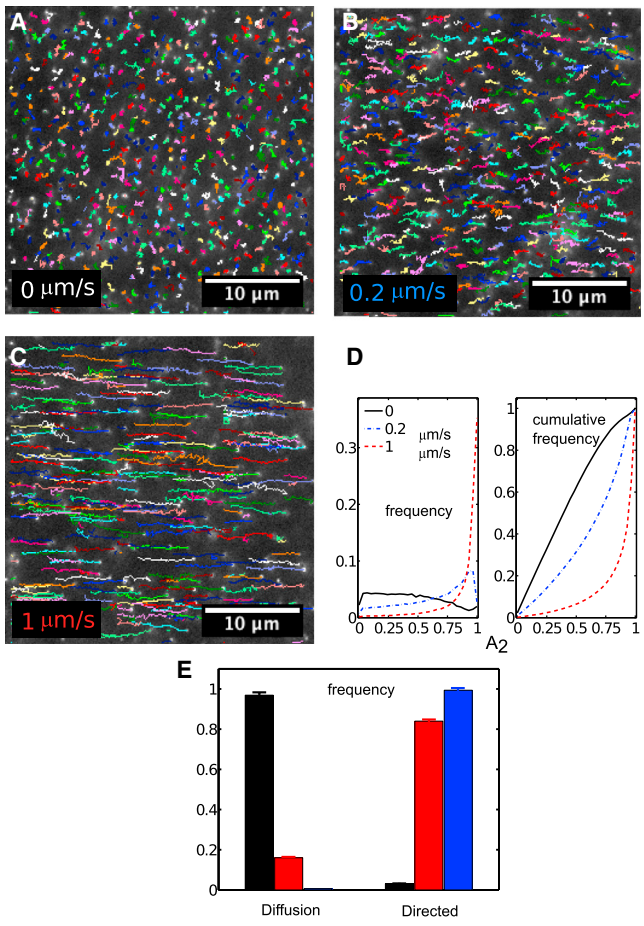

FIGURE 1 (*A–C*) SPT of fluorescent beads from three separate experiments, with.the microscope stage immobile ($N = 36{,}400$) (*A*) and moving at a constant speed of 0.2 μm/s ($N = 51{,}600$) (*B*) and 1 μm/s ($N = 39{,}700$) (*C*). (*D*) Normalized histogram of shape descriptor A_2 in each experiment. Movies S1–S3 correspond to the images in *A–C*, respectively, filmed at 10 fps for 5 s and displayed in real time. (*E*) Normalized histogram of tracks fitting either diffusive or directed-motion models.

corresponds to the typical A_2 distribution for random diffusion (25): the probability has a plateau for $A_2 \rightarrow 0$ and goes to 0 for $A_2 \rightarrow 1$. As the speed of the stage increases (directed motion), the histograms skew progressively toward $A_2 = 1$ (Fig. 1 *D*). This shows that the algorithm can properly and efficiently detect directed motion. To test the consistency of this analysis, we further studied the motion type by analyzing the MSD curves (Eq. 4) of the trajectories. We include the histogram of the tracks that fit either a random-diffusion (Eq. 5) or a directed-motion (Eq. 6) model for stage speeds of 0 μm/s, 0.2 μm/s, and 1 μm/s (Fig. 1 *E*). The corresponding values of RD (Eq. 9) are 0.03 $\pm$ 0.002, 5.2 $\pm$ 0.2, and 155 $\pm$ 20. These results show that both A_2 and MSD analyses are consistent and are able to distinguish random from directed motion.

GFP-AQP4 vesicles move similarly in polarized and nonpolarized cells

We next used this method to analyze the dynamics of protein trafficking to the BPM by examining vesicles that transport GFP-AQP4 in MDCK cells. Initially, we evaluated two different conditions: nonpolarized (isolated) cells and polarized or partially polarized cells. At steady state, we found GFP-AQP4 in punctate structures distributed throughout the cytoplasm in both polarized (Fig. 2 *A*) and nonpolarized cells (Fig. 2 *B*). In polarized cells, however, a significant amount of GFP-AQP4 is also localized to the BPM, defined as a site of contact with another cell (Fig. 2 *A*, *arrows*).

To study the movement of vesicles containing GFP-AQP4, we imaged cells and tracked the vesicles using our SPT algorithm (Fig. 2 *C* and Movie S4). We initially hypothesized that in polarized cells, the observed vesicles would be transported to the BPM in a directed fashion, whereas we expected random motion in nonpolarized cells. The statistical distribution (and its cumulative representation) of the shape descriptor A_2, time lag, mean speed, and Rg^2 are shown in Fig. 2, *D*–*G*. Based on the hypothesis above, we expected that the A_2 histogram in polarized cells would be skewed to the right with respect to nonpolarized cells. We were surprised to find that not only is the distribution of A_2 in polarized cells indistinguishable from that in nonpolarized cells, but the distribution of all the other descriptors is also indistinguishable between the two cell types (Fig. 2, *D*–*G*). We also show the normalized histogram of trajectories (Fig. 2 *H)* that fit either a random-diffusion or a directed-motion model, in which there is no significant difference in motion type between polarized and nonpolarized cells. In addition, the R_D fraction is 0.22 $\pm$ 0.01 for nonpolarized cells and 0.25 $\pm$ 0.02 for polarized cells, quantitatively confirming the lack of difference. Although we found no significant differences in the trajectories of GFP-AQP4-containing vesicles in polarized versus nonpolarized cells, it is clear that GFP-AQP4 is found on the BPM, suggesting that some yet unknown mechanism localizes it to that site.

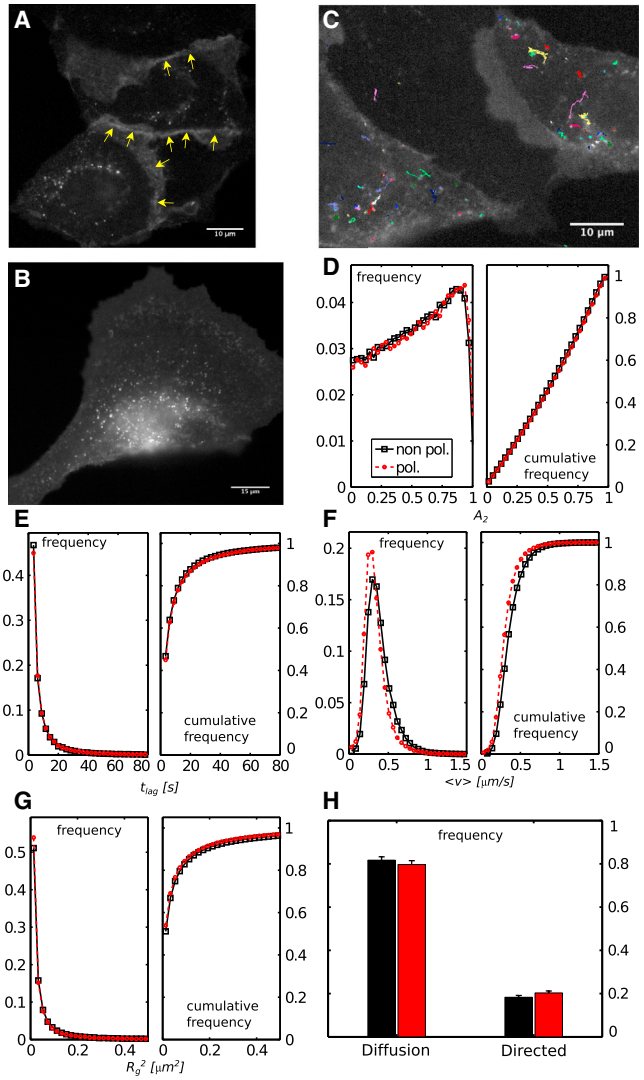

FIGURE 2 (*A* and *B*) Polarized (*A*) and nonpolarized (*B*) MDCK cells expressing GFP-AQP4. Yellow arrows point to regions of GFP-AQP4 localization. (*C*) SPT results in polarized cells in images taken at 4 fps for 6 min and 15 s (see Movie S4 for the first minute of the experiment). (*D*–*G*) Normalized histograms of descriptors in polarized cells ($N = 46{,}000$ tracks in 168 cells) and nonpolarized cells ($N = 60{,}600$ tracks in 20 cells), for shape descriptor A_2 (*D*); time lag (*E*); mean speed (*F*); and gyration radius (*G*). (*H*) Normalized histogram of tracks fitting either diffusive or directed-motion models.

Vesicles close to the plasma membrane behave in the same fashion as those farther away

Since we found that vesicles containing GFP-AQP4 in polarized cells do not move differently from those in nonpolarized cells, we explored the possibility that they behave differently according to their proximity to the BPM. We predicted that vesicles move randomly in regions farther away from the plasma membrane, but that they show directed motion toward the BPM when localized in the neighborhood close to it. We separated the vesicles tracked in polarized cells into two groups, those in regions close to the BPM

(~5 μm) and those farther away from it (Fig. 3 *A*). Contrary to our prediction, we found no difference in the statistical distribution of A_2 between the two groups (Fig. 3 *B*), as is confirmed by the fact that R_D has very similar values in both conditions (0.22 $\pm$ 0.02 far from the membrane and 0.28 $\pm$ 0.02 near it).

Vesicles move toward and away from the plasma membrane at similar rates

Regardless of the type of motion of the vesicles, we wanted to quantify the net translocation of GFP-AQP4 to the BPM. To that aim, we assessed the net distance each vesicle moved toward the BPM. By computing the orthogonal distances to the membrane from both the start (d_s) and the end (d_e) coordinates of the trajectory, we defined the descriptor $d = d_s - d_e$ (Fig. 4 *A*). Positive values of d correspond to trajectories that approach the BPM, whereas negative values indicate vesicles moving away from it. We considered only the vesicles close to the membrane (as for Fig. 3) and found that the trajectories of GFP-AQP4 vesicles show a strongly symmetrical distribution curve for d (Fig. 4 *B*), indicating that the number of tracks approaching the membrane is the same as the number moving a certain distance away from it.

In addition, we studied the orientation of the trajectories with respect to the basolateral membrane. To do this, we computed the angle α between the line orthogonal to the membrane and the orientation of the gyration ellipse for each trajectory (Fig. 4 *C*). We present a normalized histogram of α for all the trajectories close to the BM (Fig. 4, *B* and *D*). This distribution reveals that there is an increased number of tracks oriented parallel to the basolateral membrane.

GFP-AQP4 vesicle movement is not random and requires microtubules

Although we were not able to observe directed trafficking toward the BPM, the shape of the trajectories, as observed directly from the movies, is not consistent with random

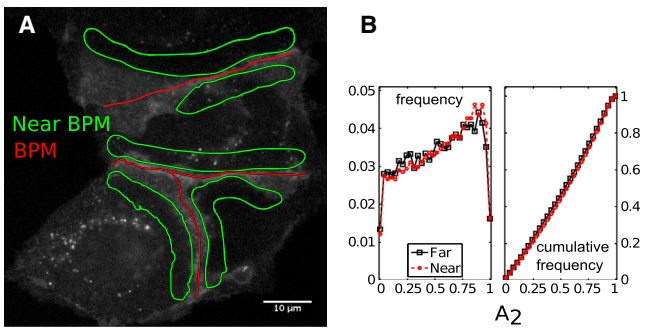

FIGURE 3 (*A*) Regions near the BPM. (*B*) Normalized histogram of shape descriptor A_2 of GFP-AQP4 vesicle trajectories in 168 polarized MDCK cells, distinguished between two regions of the cell, within ~5 μm of the BPM (N = 25,000), and outside this region (N = 21,000).

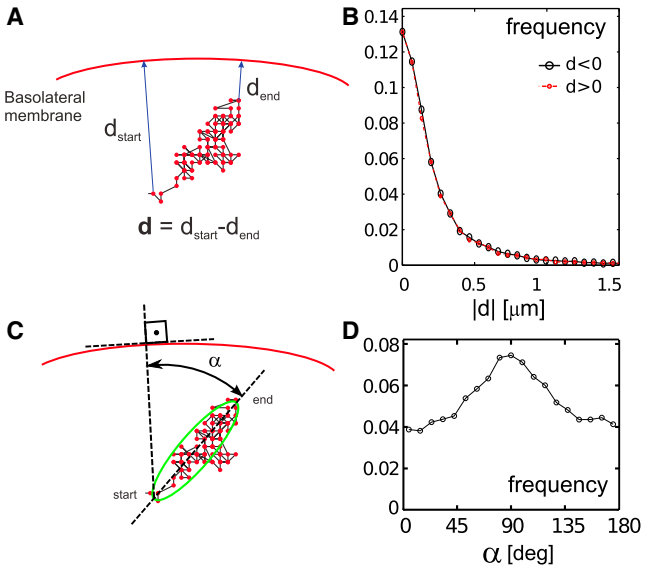

FIGURE 4 (*A*) Scheme of descriptor d. (*B*) Normalized histogram of d. (*C*) Scheme of orientation angle α. (*D*) Normalized distribution of α. Results correspond to 168 polarized cells for which only the vesicles within 5 μm of the BPM are considered (N = 25,000).

diffusion. On the contrary, vesicles move following one-dimensional guiding structures. To study this quantitatively, we compared the set of trajectories of polarized cells (Fig. 2 *B*, N = 46,000) with the same number of numerically simulated random walks. For realistic comparison, we generated trajectories with random fluctuations of direction and instantaneous speed while matching, one by one, the time lag and average speed of the experimental tracks. As expected, experimental trajectories are more elongated than simulated random trajectories (Fig. 5 *A*), and a greater fraction of them fit a directed-motion model (Fig. 5 *B*) (R_D = 0.25 $\pm$ 0.02 for the experimental trajectories and 0.04 $\pm$ 0.004 for the simulated diffusing tracks). This supports the hypothesis that GFP-AQP4 vesicles are actively transported, possibly along cytoskeleton fibers such as microtubules or actin filaments.

Transport along microtubules involves molecular motors, many of which have been implicated in polarized trafficking. Although most take part in apical delivery, some have been implicated in basolateral transport. For example, it has been shown that the kinesin family member KIFC3 is implicated in the delivery of influenza HA and anexin 13b to the apical membrane (28). Analogously, another kinesin family member, KIF5B, transports p75 to the apical membrane (29). Regarding basolateral transport, it was observed that immunodepletion of the heavy chain of cytosolic kinesin (using an SUK-4 antibody) inhibits delivery of vesicular stomatitis virus glycoprotein in MDCK cells (6). Although there is a plethora of works that implicate molecular motors in protein trafficking, the dynamic details of this kind of transport are scarce.

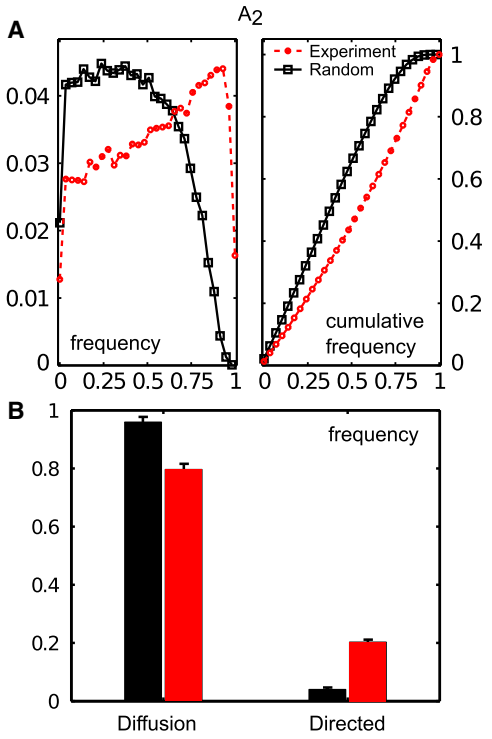

FIGURE 5 Comparison between experimental trajectories ($N = 46{,}000$ vesicles in 168 polarized cells) and numerically simulated randomly diffusing trajectories. (*A*) Normalized histograms of shape parameter A_2. (*B*) Trajectories fitting either diffusive or directed-motion models. Each trajectory in the simulated set is paired to one experimental trajectory by matching the time lag and mean speed.

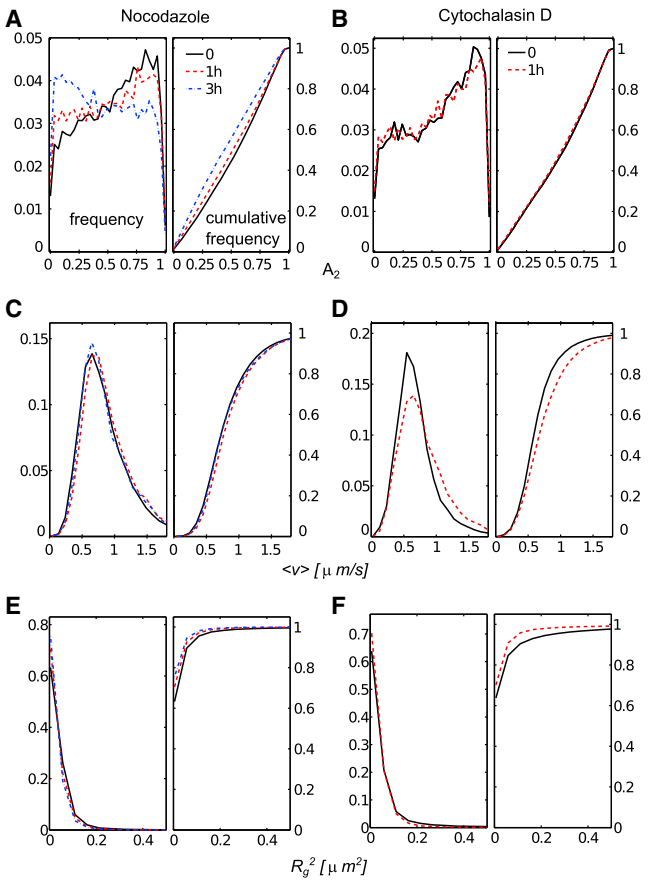

FIGURE 6 Pharmacological study of GFP-AQP4-positive vesicle dynamics using nocodazole (*A*, *C*, and *E*) on 50 cells at 0 h (N = 19,000), 1 h ($N = 16{,}000$), and 3 h ($N = 12{,}000$) after drug application, and cytochalasin D (*B*, *D*, and *F*) on 20 cells at 0 h ($N = 11{,}000$ tracks) and 1 h ($N = 9000$ tracks) after drug application. Effects of the pharmacological treatments on descriptors A_2 (*A* and *B*), average velocity (*C* and *D*), and gyration radius (*E* and *F*) are shown as histograms (*left*) and cumulative histograms (*right*).

To gain more insight into the role of the cytoskeleton in the trafficking of vesicles to the basolateral membrane, we studied the shape of GFP-AQP4 vesicle trajectories after pharmacologically disrupting microtubules or F-actin. We seeded MDCK cells stably expressing GFP-AQP4 on glass-bottomed dishes and imaged them live the next day. The same regions were imaged 1 h and 3 h after adding nocodazole to the cell culture media to a concentration of 33 μM. The statistical distribution of A_2 (Fig. 6 *A*) skews progressively toward 0 as microtubules are disrupted. More precisely, we found that as the fraction of disrupted microtubules increases, a higher proportion of vesicles stop following elongated structures and begin undergoing random diffusion. This result is consistent with the hypothesis that GFP-AQP4-containing vesicles are transported along microtubules. The average speed (Fig. 6 *C*) shows no change, and there is a marginal decrease in the gyration radius as microtubules are disrupted (Fig. 6 *E*). We have verified the disruption of microtubules by studying confocal sections of MDCK cells stained with anti-tubulin antibody at three different time points (0 h, 1 h, and 3 h) after addition of nocodazole (Fig. 7, *A–C*). We quantified the filamentous content of a set of cells from different fields of view throughout each sample, using the algorithm described in the Supporting Material. A representative image is shown (Fig. 7, *D–F*) magnified (28×28 μm^2) from the fields of view previously shown (Fig. 7, *A–C*). Here, the quantification is depicted in 16 color-coded square regions. Altogether, these results show that microtubules are disrupted partially at 1 h and more significantly at 3 h after nocodazole treatment (Fig. 7 *G*), which is consistent with observations of the transition from linear-like to random transport (Fig. 6 *A*).

To test whether the guided motion of the vesicles is also due to transport along actin filaments, we used cytochalasin D to disrupt F-actin fibers. In this case, we imaged a set of cells in conditions analogous to experimental conditions with nocodazole. We imaged cells at time 0, and 1 h after adding cytochalasin D to the media to a final concentration of 0.25 μg/ml, we imaged the same cells again. Compared to our previous observations of disrupted microtubules, the disruption of F-actin had no effect on the shape of the trajectories, as vesicles kept moving mostly in the same one-dimensional way (Fig. 6 *B*); this suggests that they don't

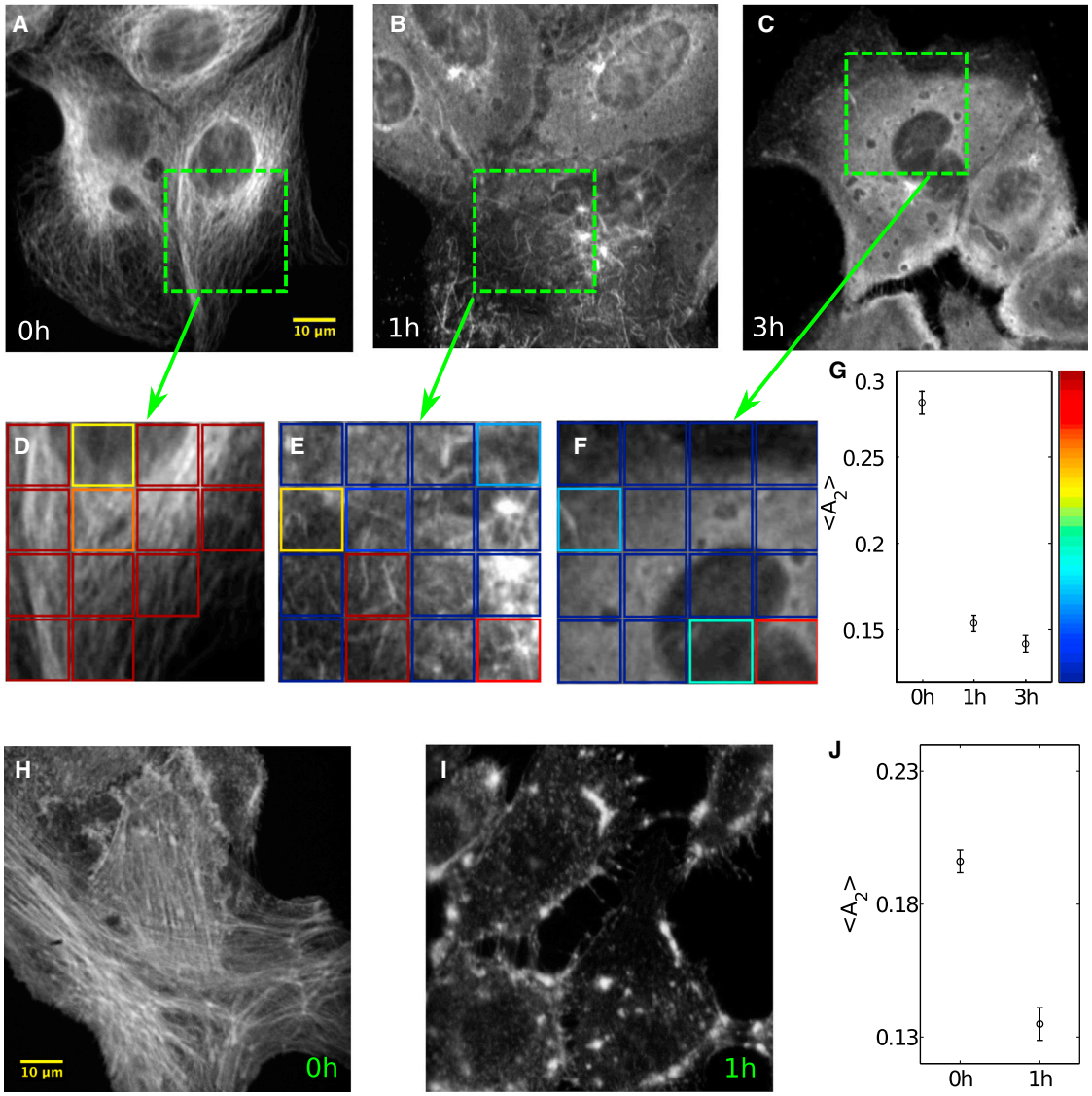

FIGURE 7 Quantification of the disruption of microtubules upon nocodazole treatment and actin filaments upon cytochalasin D treatment. (*A–C*) Confocal sections of MDCK cells stained with anti-tubulin antibody 0 h, 1 h, and 3 h after the addition of nocodazole. (*D–F*) Examples of quantification of filamentous contents within the dashed 7×7-μm^2 regions indicated in *A–C*. The color of squares indicates the A_2 value according to the color scale in *G*. (*G*) Mean values of A_2, quantifying the contents of microtubules at 0 h (28 cells), 1 h (37 cells), and 3 h (42 cells) from five different fields of view for each condition (see Supporting Material). (*H* and *I*) Confocal sections of MDCK cells stained with phalloidin after 0 h and 1 h, respectively, of applying cytochalasin D. (*J*) Mean values of A_2, quantifying actin filaments at 0 h (85 cells in 13 fields of view) and 1 h (57 cells in nine fields of view). Bars in *G* and *J* indicate the mean ± SE.

move along actin filaments. It should be noted that there is a marginal increase of the average speed (Fig. 6 *D*) and also a minor decrease of the gyration radius (Fig. 6 *F*). The degree of disruption of actin filaments was verified by confocal images of MDCK cells stained with phalloidin after cytochalasin D treatment at 0 h and 1 h (see Fig. 7, *H–J*).

DISCUSSION

To better understand how cells sort and traffic AQP4 to basolateral membranes, we studied the dynamics of GFP-AQP4-transporting vesicles in nonpolarized and polarized MDCK cells with fast time-lapse imaging and SPT. We studied a large number of vesicles ($>10^4$) in a large number of cells (typically 168), rendering reliable results by reducing statistical bias to a minimum.

We found no differences in vesicle dynamics between polarized and nonpolarized cells. Even in polarized cells, vesicles near the BPM move in ways undistinguishable from vesicle movements in other regions. Furthermore, the protein transport toward and away from the BPM occurs at similar rates, showing that movement of the vesicles does not show any tendency to approach that membrane. However, we did observe that GFP-AQP4 is localized to

the BPM in polarized cells. This suggests that the mechanisms that drive the basolateral localization of GFP-AQP4 do not include modifying vesicle dynamics when cells polarize. Instead, it is possible that the machinery that controls specific targeting of GFP-AQP4 to the BPM relies on the composition of a targeting patch, consisting of the exocyst complex and SNAREs (30), as has been proposed (31). This kind of mechanism has been suggested for other basolateral proteins (32,33), which in turn is consistent with the idea that the address code of the vesicles specifies only the target membrane and not the intermediate path (34).

Although GFP-AQP4 vesicles are not directed straight to the BPM, they move along elongated trajectories. This suggests that rather than diffusing in the cytosol, vesicles are actively transported throughout the cell along cytoskeleton fibers. The elongated shape of their trajectories is lost when microtubules are disrupted with nocodazole, suggesting that the movement of GFP-AQP4-containing vesicles is guided by microtubules. The transport of proteins to the plasma membrane along microtubules has also been reported in nonpolarizable cells. For example, it was shown in HeLa and rat hepatic epithelial cells (WB-F344) that vesicles delivering connexin-based hemichannels travel from the region of the Golgi via microtubules to sites of established cell-cell contacts (35).

Over the last decade, it has been suggested that the actin cytoskeleton plays an active role in basolateral trafficking, as it does for trafficking proteins in yeast (7,36,37). It has even been reported that F-actin plays a primary role in localizing AQP4 to the plasma membrane during cell adhesion in astrocytes (17). Our results, however, show that the dynamics of GFP-AQP4 vesicles is not significantly guided along actin filaments, because after F-actin depolymerization, the elongated shape of the trajectories remains unchanged. Results similar to ours have been reported for the trafficking of secretory organelles in primary human umbilical vein endothelial cells (38). In this study, they show that the long-range vesicle translocation is essentially microtubule-dependent, whereas actin decreases their frequency and, in some cases, their velocity. As mentioned before, our results support a role for microtubules in the trafficking of GFP-AQP4 vesicles as we did not observe significant effects by depolarizing actin filaments. Therefore, it is possible that different cell types use different cytoskeleton elements to traffic proteins to the basolateral membrane or that the F-actin cytoskeleton may be involved, at some point, in the trafficking of AQP4 to the BPM, but it does not play a role in the dynamics of the vesicles observed in this study.

The observations that microtubule disruption yields an increased number of vesicles undergoing random diffusion and that the movement toward the BPM is balanced suggest that vesicles move in both directions of the microtubules, stochastically. Bidirectional transport along microtubules was proposed a long time ago and has been thoroughly reviewed (39,40). However, to the best of our knowledge, it was never studied quantitatively regarding apical versus basolateral trafficking in polarized cells. The translocation of proteins along the microtubule depends on molecular motors that pull vesicles to either the plus or minus end of the filaments. For bidirectional movement, however, it has been suggested that the direction of the movement is the result of the force's balance between opposing motors (41,42). In the case of GFP-AQP4, it seems that this balance is stochastic (and probably dynamic), because the movement of all the vesicles is not biased in any direction. This dynamics has been also observed in secretory pathways (38,43) and, of more relevance, in the basolateral transport of AQP3, where it was qualitatively observed that the vesicles travel in linear paths, with several pauses and changes of direction (32).

It was initially argued that microtubules have an important effect on apical trafficking but seldom intervene in basolateral sorting (4,7,33,44–47). Nonetheless, the importance of microtubules in basolateral trafficking seems to be controversial (21,48), as some authors have reported that microtubules are involved in basolateral delivery of proteins (6,49). Indeed, it has been shown that a microtubule-interacting protein (PAT1) recognizes a basolateral sorting signal (50), and it was reported that AQP3 basolateral transport was impaired by disruption of microtubules, supporting an important role for these microfibers in basolateral trafficking (32). One surprise from our study was the lack of direct transport to the BPM, even though AQP4 may be transported along microtubules. As suggested at the beginning of this section, one possible model for basolateral trafficking of AQP4 is that the signal determining the destination membrane is in the neighborhood of the membrane itself, and that vesicles attach stochastically upon contact. In this context, active transport along microtubules may increase the contact frequency between the vesicles and the membrane, thereby increasing the probability of the protein fusing with it. As has been suggested, transport along microtubules may regulate the efficiency rather than the fidelity of vesicle delivery (5,49).

SUPPORTING MATERIAL

Four movies, one figure, and supplementary methods are available at http://www.biophysj.org/biophysj/supplemental/S0006-3495(13)00684-X.

We thank Dr. Craig Mandato (McGill University, Montreal, Canada) for providing anti-tubulin antibody and phalloidin.

This work was funded by grants from the Fondation de l'Hôpital Maisonneuve Rosemont (La néphrologie et son Impact) to S.C. and S.L., and the National Sciences and Engineering Research Council (NSERC) to S.C. S.C. and S.L. are recipients of salary awards from Fonds de la Recherche en Santé du Quebec (FRSQ). J.M. is a recipient of a postdoctoral fellowship from the Fondation de l'Hôpital Maisonneuve-Rosemont (La néphrologie et son Impact).

REFERENCES

1. Cao, X., M. A. Surma, and K. Simons. 2012. Polarized sorting and trafficking in epithelial cells. *Cell Res.* 22:793–805.
2. Fölsch, H., P. E. Mattila, and O. A. Weisz. 2009. Taking the scenic route: biosynthetic traffic to the plasma membrane in polarized epithelial cells. *Traffic.* 10:972–981.
3. Alberts, B. 2008. Molecular Biology of the Cell. Garland Science, New York.
4. Apodaca, G., L. I. Gallo, and D. M. Bryant. 2012. Role of membrane traffic in the generation of epithelial cell asymmetry. *Nat. Cell Biol.* 14:1235–1243.
5. Mellman, I., and W. J. Nelson. 2008. Coordinated protein sorting, targeting and distribution in polarized cells. *Nat. Rev. Mol. Cell Biol.* 9:833–845.
6. Lafont, F., J. K. Burkhardt, and K. Simons. 1994. Involvement of microtubule motors in basolateral and apical transport in kidney cells. *Nature.* 372:801–803.
7. Rodriguez-Boulan, E., G. Kreitzer, and A. Müsch. 2005. Organization of vesicular trafficking in epithelia. *Nat. Rev. Mol. Cell Biol.* 6: 233–247.
8. Krane, C. M., and D. L. Goldstein. 2007. Comparative functional analysis of aquaporins/glyceroporins in mammals and anurans. *Mamm. Genome.* 18:452–462.
9. King, L. S., D. Kozono, and P. Agre. 2004. From structure to disease: the evolving tale of aquaporin biology. *Nat. Rev. Mol. Cell Biol.* 5: 687–698.
10. Agre, P., M. Bonhivers, and M. J. Borgnia. 1998. The aquaporins, blueprints for cellular plumbing systems. *J. Biol. Chem.* 273:14659–14662.
11. Ecelbarger, C. A., J. Terris, …, M. A. Knepper. 1995. Aquaporin-3 water channel localization and regulation in rat kidney. *Am. J. Physiol.* 269:F663–F672.
12. Terris, J., C. A. Ecelbarger, …, S. Nielsen. 1995. Distribution of aquaporin-4 water channel expression within rat kidney. *Am. J. Physiol.* 269:F775–F785.
13. Nakahama, K., A. Fujioka, …, Y. Shigeyoshi. 2002. A role of the C-terminus of aquaporin 4 in its membrane expression in cultured astrocytes. *Genes Cells.* 7:731–741.
14. Madrid, R., S. Le Maout, …, J. Mérot. 2001. Polarized trafficking and surface expression of the AQP4 water channel are coordinated by serial and regulated interactions with different clathrin-adaptor complexes. *EMBO J.* 20:7008–7021.
15. Kadohira, I., Y. Abe, …, M. Yasui. 2008. Phosphorylation in the C-terminal domain of Aquaporin-4 is required for Golgi transition in primary cultured astrocytes. *Biochem. Biophys. Res. Commun.* 377: 463–468.
16. Guan, X. G., W. H. Su, …, T. H. Ma. 2010. NPA motifs play a key role in plasma membrane targeting of aquaporin-4. *IUBMB Life.* 62: 222–226.
17. Nicchia, G. P., A. Rossi, …, M. Svelto. 2008. Actin cytoskeleton remodeling governs aquaporin-4 localization in astrocytes. *Glia.* 56: 1755–1766.
18. Carmosino, M., G. Procino, …, G. Valenti. 2007. Trafficking and phosphorylation dynamics of AQP4 in histamine-treated human gastric cells. *Biol. Cell.* 99:25–36.
19. Moeller, H. B., R. A. Fenton, …, N. Macaulay. 2009. Vasopressin-dependent short-term regulation of aquaporin 4 expressed in *Xenopus* oocytes. *Neuroscience.* 164:1674–1684.
20. Rustom, A., M. Bajohrs, …, H. H. Gerdes. 2002. Selective delivery of secretory cargo in Golgi-derived carriers of nonepithelial cells. *Traffic.* 3:279–288.
21. Toomre, D., P. Keller, …, K. Simons. 1999. Dual-color visualization of trans-Golgi network to plasma membrane traffic along microtubules in living cells. *J. Cell Sci.* 112:21–33.
22. Crocker, J. C., and D. G. Grier. 1996. Methods of digital video microscopy for colloidal studies. *J. Colloid Interface Sci.* 179:298–310.
23. Mazzaferri, J., D. Kunik, …, S. Costantino. 2011. Analyzing speckle contrast for HiLo microscopy optimization. *Opt. Express.* 19:14508–14517.
24. Fujita, H., H. Hatakeyama, …, M. Kanzaki. 2010. Identification of three distinct functional sites of insulin-mediated GLUT4 trafficking in adipocytes using quantitative single molecule imaging. *Mol. Biol. Cell.* 21:2721–2731.
25. Saxton, M. J. 1993. Lateral diffusion in an archipelago. Single-particle diffusion. *Biophys. J.* 64:1766–1780.
26. Levi, V., and E. Gratton. 2007. Exploring dynamics in living cells by tracking single particles. *Cell Biochem. Biophys.* 48:1–15.
27. Bevington, P. R., and D. K. Robinson. 2003. Data Reduction and Error Analysis for the Physical Sciences. McGraw-Hill, Boston.
28. Noda, Y., Y. Okada, …, N. Hirokawa. 2001. KIFC3, a microtubule minus end-directed motor for the apical transport of annexin XIIIb-associated Triton-insoluble membranes. *J. Cell Biol.* 155:77–88.
29. Jaulin, F., X. Xue, …, G. Kreitzer. 2007. Polarization-dependent selective transport to the apical membrane by KIF5B in MDCK cells. *Dev. Cell.* 13:511–522.
30. He, B., and W. Guo. 2009. The exocyst complex in polarized exocytosis. *Curr. Opin. Cell Biol.* 21:537–542.
31. Grindstaff, K. K., C. Yeaman, …, W. J. Nelson. 1998. Sec6/8 complex is recruited to cell-cell contacts and specifies transport vesicle delivery to the basal-lateral membrane in epithelial cells. *Cell.* 93:731–740.
32. Nejsum, L. N., and W. J. Nelson. 2007. A molecular mechanism directly linking E-cadherin adhesion to initiation of epithelial cell surface polarity. *J. Cell Biol.* 178:323–335.
33. Kreitzer, G., J. Schmoranzer, …, E. Rodriguez-Boulan. 2003. Three-dimensional analysis of post-Golgi carrier exocytosis in epithelial cells. *Nat. Cell Biol.* 5:126–136.
34. Rothman, J. E. 1994. Mechanisms of intracellular protein transport. *Nature.* 372:55–63.
35. Shaw, R. M., A. J. Fay, …, L. Y. Jan. 2007. Microtubule plus-end-tracking proteins target gap junctions directly from the cell interior to adherens junctions. *Cell.* 128:547–560.
36. Au, J. S. Y., C. Puri, …, F. Buss. 2007. Myosin VI is required for sorting of AP-1B-dependent cargo to the basolateral domain in polarized MDCK cells. *J. Cell Biol.* 177:103–114.
37. Sheff, D. R., R. Kroschewski, and I. Mellman. 2002. Actin dependence of polarized receptor recycling in Madin-Darby canine kidney cell endosomes. *Mol. Biol. Cell.* 13:262–275.
38. Manneville, J. B., S. Etienne-Manneville, …, M. Ferenczi. 2003. Interaction of the actin cytoskeleton with microtubules regulates secretory organelle movement near the plasma membrane in human endothelial cells. *J. Cell Sci.* 116:3927–3938.
39. Welte, M. A. 2004. Bidirectional transport along microtubules. *Curr. Biol.* 14:R525–R537.
40. Hayden, J. H. 1988. Microtubule-associated organelle and vesicle transport in fibroblasts. *Cell Motil. Cytoskeleton.* 10:255–262.
41. Müller, M. J. I., S. Klumpp, and R. Lipowsky. 2008. Tug-of-war as a cooperative mechanism for bidirectional cargo transport by molecular motors. *Proc. Natl. Acad. Sci. USA.* 105:4609–4614.
42. Hendricks, A. G., E. Perlson, …, E. L. F. Holzbaur. 2010. Motor coordination via a tug-of-war mechanism drives bidirectional vesicle transport. *Curr. Biol.* 20:697–702.
43. Wacker, I., C. Kaether, …, H. H. Gerdes. 1997. Microtubule-dependent transport of secretory vesicles visualized in real time with a GFP-tagged secretory protein. *J. Cell Sci.* 110:1453–1463.
44. Cole, N. B., and J. Lippincott-Schwartz. 1995. Organization of organelles and membrane traffic by microtubules. *Curr. Opin. Cell Biol.* 7:55–64.
45. van Zeijl, M. J., and K. S. Matlin. 1990. Microtubule perturbation inhibits intracellular transport of an apical membrane glycoprotein in a

substrate-dependent manner in polarized Madin-Darby canine kidney epithelial cells. *Cell Regul.* 1:921–936.

46. Breitfeld, P. P., W. C. McKinnon, and K. E. Mostov. 1990. Effect of nocodazole on vesicular traffic to the apical and basolateral surfaces of polarized MDCK cells. *J. Cell Biol.* 111:2365–2373.

47. Li, R., and G. G. Gundersen. 2008. Beyond polymer polarity: how the cytoskeleton builds a polarized cell. *Nat. Rev. Mol. Cell Biol.* 9: 860–873.

48. Müsch, A. 2004. Microtubule organization and function in epithelial cells. *Traffic.* 5:1–9.

49. Grindstaff, K. K., R. L. Bacallao, and W. J. Nelson. 1998. Apiconuclear organization of microtubules does not specify protein delivery from the trans-Golgi network to different membrane domains in polarized epithelial cells. *Mol. Biol. Cell.* 9:685–699.

50. Zheng, P., J. Eastman, …, S. W. Pimplikar. 1998. PAT1, a microtubule-interacting protein, recognizes the basolateral sorting signal of amyloid precursor protein. *Proc. Natl. Acad. Sci. USA.* 95:14745–14750.